Front. Phys.
https://doi.org/10.15302/frontphys.2027.052202
CN 11-5994/O4
ISSN 2095-0462

RESEARCH ARTICLE

Stable (2+1)-dimensional soliton and breather molecules in a cold Rydberg atomic gas

Lu Qin[1], Hairu Zhai[1], Lu Liu[1], Zeyun Shi[2*], Yingying Zhang[1†], Zunlue Zhu[1], Xingdong Zhao[1‡], Wu-Ming Liu[1], Boris A. Malomed[3,4]

[1]School of Physics, Henan Normal University, Xinxiang 453007, China
[2]School of Artificial Intelligence, Hubei University of Automotive Technology, Shiyan 442000, China
[3]Department of Physical Electronics School of Electrical and Computer Engineering Faculty of Engineering Tel Aviv University Ramat Aviv, Tel Aviv 6997801, Israel
[4]Instituto de Alta Investigación Universidad de Tarapacá Casilla 7D, Arica1 000000, Chile
Corresponding authors. E-mail: *shizy@huat.edu.cn, †yyzwuli415@163.com, ‡phyzhxd@gmail.com
Received September 25, 2026; accepted November 16, 2026

Abstract

We investigate the formation of stable (2+1)-dimensional [(2+1)D] spatial-domain optical soliton molecules (SMs) and breather molecules (BMs) in a gas of Rydberg atoms, highlighting the role of the nonlocal nonlinearity, which is generated by the electromagnetically induced transparency (EIT) in the Rydberg medium. The setting supports diverse species of large-size polygonal SMs, including rectangular and oblique rhombuses, checkerboard cells, and hexagons. The analysis identifies two distinct formation regimes. In the case of moderately nonlocality, the long-range interactions alone stabilize the SMs in the static form. In contrast, in the strongly nonlocal regime, initially imposed rotation is required to generate a centrifugal force that counteracts the strong attraction, resulting in stably rotating SMs. The rotation period can be controlled by adjusting the system's parameters. Furthermore, appropriate initial velocities can induce inherent breathing dynamics in the solitons, leading to the formation of BMs. Tuning the initial velocity, one can control the evolution of SMs and BMs and even realize their mutual conversion. Our study offers a new scheme for engineering SMs and BMs, and suggests new possibilities for the design of data processing and transmission in optical systems.

Keywords cold Rydberg atom, nonlocal optical nonlinearity, soliton molecules, breather molecules

© Higher Education Press 2026

Just Accepted

This is a "Just Accepted" manuscript, which has been examined by the peer-review process and has been accepted for publication. A "Just Accepted" manuscript is published online shortly after its acceptance, which is prior to technical editing and formatting and author proofing. Higher Education Press (HEP) provides "Just Accepted" as an optional and free service which allows authors to make their results available to the research community as soon as

possible after acceptance. After a manuscript has been technically edited and formatted, it will be removed from the "Just Accepted" Web site and published as an Online First article. Please note that technical editing may introduce minor changes to the manuscript text and/or graphics which may affect the content, and all legal disclaimers that apply to the journal pertain. In no event shall HEP be held responsible for errors or consequences arising from the use of any information contained in these "Just Accepted" manuscripts. To cite this manuscript please use its Digital Object Identifier (DOI®), which is identical for all formats of publication.

Stable (2+1)-dimensional soliton and breather molecules in a cold Rydberg atomic gas

Lu Qin[1], Hairu Zhai[1], Lu Liu[1], Zeyun Shi[2*], Yingying Zhang[1†], Zunlue Zhu[1], Xingdong Zhao[1‡], Wu-Ming Liu[1], and Boris A. Malomed[3,4]

[1] *School of Physics, Henan Normal University, Xinxiang 453007, China*

[2] *School of Artificial Intelligence, Hubei University of Automotive Technology, Shiyan 442000, China*

[3] *Department of Physical Electronics School of Electrical and Computer Engineering Faculty of Engineering Tel Aviv University Ramat Aviv, Tel Aviv 6997801, Israel*

[4] *Instituto de Alta Investigación Universidad de Tarapacá Casilla 7D, Arica1 000000, Chile**

(Dated: November 1, 2026)

We investigate the formation of stable (2+1)-dimensional [(2+1)D] spatial-domain optical soliton molecules (SMs) and breather molecules (BMs) in a gas of Rydberg atoms, highlighting the role of the nonlocal nonlinearity, which is generated by the electromagnetically induced transparency (EIT) in the Rydberg medium. The setting supports diverse species of large-size polygonal SMs, including rectangular and oblique rhombuses, checkerboard cells, and hexagons. The analysis identifies two distinct formation regimes. In the case of moderately nonlocality, the long-range interactions alone stabilize the SMs in the static form. In contrast, in the strongly nonlocal regime, initially imposed rotation is required to generate a centrifugal force that counteracts the strong attraction, resulting in stably rotating SMs. The rotation period can be controlled by adjusting the system's parameters. Furthermore, appropriate initial velocities can induce inherent breathing dynamics in the solitons, leading to the formation of BMs. Tuning the initial velocity, one can control the evolution of SMs and BMs and even realize their mutual conversion. Our study offers a new scheme for engineering SMs and BMs, and suggests new possibilities for the design of data processing and transmission in optical systems.

I. INTRODUCTION

Solitons, alias self-localized nonlinear waves, have attracted great attention in hydrodynamics and plasmas [1], optics [2–7], superconductivity [8], and quantum systems [9–11]. Nowadays, stable bound states of solitons [12–18] that arise from the balance of attractive and repulsive interactions between adjacent ones, also known as soliton molecules (SMs) [19–23], have become a new research frontier. Their unique properties offer a wide range of potential applications in various physical systems, including mode-locked fiber lasers [24], dispersion management optical fiber [25], optical microresonators [26], exciton-polariton superfluids [27], Bose-Einstein condensates (BEC) [28, 29], etc. In particular, SMs provide promising applications in optics, including the design of new laser schemes [30], optical switches [31–33], coherent frequency combs [26], advanced optical telecommunications [34], data encoding and transmission [19, 35–41], etc.

Earlier work on SMs was confined to one-dimensional (1D) settings with local nonlinearity, exemplified by temporal SMs in fiber lasers [42–48]. In local nonlinear systems, SMs form solely through short-range (contact) interactions, making the creation of large-size SMs in 1D and the transition to 2D and 3D a challenging problem, due to instabilities emerging in these cases. Indeed, unlike 1D solitons, which normally appear as stable modes, the stability of 2D and 3D solitons is a fundamental problem, as the usual cubic self-focusing gives rise to the critical and supercritical collapse in the 2D and 3D space, respectively [49–53]. Therefore, devising physically viable stabilization mechanisms for 2D and 3D solitons and their bound states remains a major challenge. Nevertheless, research has confirmed the existence of stable multi-dimensional solitons in relatively complex physical systems [54–56]. Theoretically, 2D solitons have been demonstrated in media with competing nonlinearities [57, 58], as well as in systems involving local nonlinearity combined with an external nonlinear potential [59]. Experimentally, stable 2D solitons have been observed in optical media with cubic-quintic nonlinearity [60], and various types of solitons-like modes ("quantum droplets") have been identified in BEC [61]. Multi-dimensional solitons and their bound states in the form of the corresponding SMs remain a relevant topic for theoretical and experimental studies [62].

Recently, it has been shown that cold atomic gases steered by laser fields provide an appropriate ground for studying multi-dimensional solitons [63–69]. In particular, by coupling light to highly excited Rydberg states [63, 70, 71], strong and long-range interactions between Rydberg atoms can be induced by light fields through the effect of electromagnetically induced transparency (EIT) [72], thus generating strong nonlocal nonlinearity [70, 73]. Actually, the Rydberg-Rydberg interactions are strong even at the single-photon level [63, 70, 71]. Photonic dimers and three-photon bound states have been observed under the action of strong optical nonlinearities [73, 74]. Such bound states of photons can be viewed as quantum solitons, and they may be used

* shizy@huat.edu.cn
† yyzwuli415@163.com
‡ phyzhxd@gmail.com

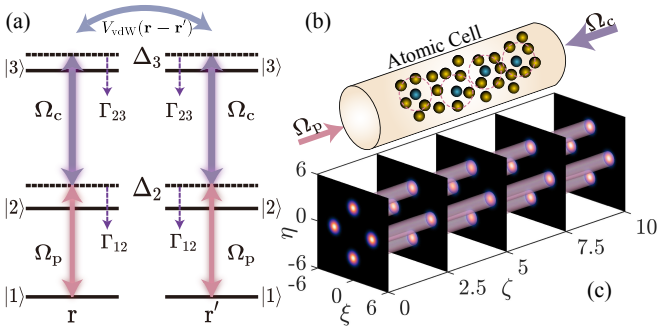


FIG. 1. (a) The energy-level diagram and excitation scheme for ladder-type three-level atoms. A weak probe optical field Ω_p drives the transition $|1\rangle \leftrightarrow |2\rangle$. A strong control laser field Ω_c drives the transition $|2\rangle \leftrightarrow |3\rangle$. In the Rydberg state $|3\rangle$, atoms strongly interact through the van der Waals potential $V_{\rm vdW}(\mathbf{r}'-\mathbf{r}) = -\hbar C_6/|\mathbf{r}'-\mathbf{r}|^6$. Δ_α are the detunings, and $\Gamma_{\alpha\beta}$ ($\alpha < \beta$) are the spontaneous-emission decay rates. (b) The long-range interaction between Rydberg atoms blocks the excitation of the atoms within the blockade spheres (indicated by the red dashed circles). In each blocked sphere only one Rydberg atom (a small dark-blue sphere) is excited and other atoms (small dark-yellow spheres) cannot be excited. The red and purple arrows indicates the propagation direction of the probe and control fields. (c) The contactless interaction between four optical solitons, which form a stable 2×2 rhombic SM, exhibiting no apparent distortion in the course of the propagation.

for the implementation of single-photon switching [75], photon-photon gates [76], and all-optical deterministic quantum logic [77], as well as for studies of many-body phenomena with strongly correlated photons [78].

Using the Rydberg nonlocal nonlinearity, it has been shown that SMs and vortex molecules (bound states of solitary vortices) can be generated and stored in the Rydberg atomic gas [22]. However, the underlying mechanisms of the formation of SMs and breather molecules (BMs) in these settings have not yet been fully understood. In particular, a remaining open question is how to design various SM and BM states in such systems. With its easily adjustable parameters, the Rydberg atomic medium allows the nonlocality ($\sigma \equiv R_{\rm b}/R_0$) to be continuously tuned from the local limit to the strongly nonlocal one, $R_{\rm b}$ and R_0 being the characteristic length of the Rydberg nonlinearity and beam width, respectively.

In this work, we address mechanisms governing the formation of stable (2+1)D optical SMs and BMs for different nonlocality degrees. Specifically, we examine how the initial velocity of circular motion, which may be imposed onto the Rydberg-EIT medium, affects the resulting rotation period of SMs and breathing period of BMs. We find that the giant nonlocal optical nonlinearity supports a variety of SM configurations, such as rectangular and oblique rhombic ones, checkerboard cells, and hexagons. They feature a large size and can be efficiently manipulated by tuning the nonlocality degree of the nonlinearity. We analyze the binding energy (BE) of the multisoliton interaction, proceeding from weak to strong nonlocality. Stable SMs can be formed by long-range interactions between quiescent solitons. On the other hand, in the strongly nonlocal regime, the SMs are supported by the balance of strong attractive interactions and the centrifugal force induced by the orbital motion of the interacting solitons, the rotation period being controllable by adjusting the system's parameters. Furthermore, the rotational motion maintains periodic centrifugal and centripetal "breathings" of the solitons, which may bind themselves into BMs. By tuning the initial velocity of the solitons, one can manipulate the evolution of the SMs and BMs and realize their mutual conversion. The numerical results, which agree very well with analytical predictions, reveal roles played by the nonlocality degree and initial velocity in the generation of the SMs and BMs, and provide a scenario for manipulating their size, rotation period, and breathing characteristics. Thus, the present study offers a new scheme for engineering diverse SM species, that may find applications in data processing and transmission in optical systems.

II. THE MODEL AND LIGHT-PROPAGATION EQUATIONS

A. The physical model

We start by considering a laser-cooled, dilute three-level atomic gas interacting with the combination of a weak probe optical field, driving the transition $|1\rangle \leftrightarrow |2\rangle$ (with half-Rabi frequency Ω_p and central frequency ω_p), and a strong control laser field, driving the transition $|2\rangle \leftrightarrow |3\rangle$ (with half-Rabi frequency Ω_c and central frequency ω_c); see Fig. 1(a). Detunings Δ_α ($\alpha = 2, 3$) define the difference between the laser frequency and atomic transitions, while $\Gamma_{\alpha\beta}$ are rates of the spontaneous emission decay $|\beta\rangle \to |\alpha\rangle$.

In this setting, level $|3\rangle$ represents a high-lying Rydberg state. The interaction between two Rydberg atoms, located at positions $\mathbf{r}$ and $\mathbf{r}'$, is accounted for by the van der Waals potential $V_{\rm vdW} = -\hbar C_6/|\mathbf{r}' - \mathbf{r}|^6$, with the dispersion coefficient C_6 [65]. When light propagates in the medium, the Rydberg excitation in a vicinity of a Rydberg atom is strongly suppressed, due to the long-range Rydberg-Rydberg interaction – see Fig. 1(b). The Rydberg blockade leads to nonlocal nonlinear optically-mediated interactions [70]. Note that, in the excitation scheme shown in Fig. 1(a), the transition $|1\rangle \to |2\rangle \to |3\rangle$ forms a ladder-shaped Rydberg-EIT.

Under the electric-dipole and rotating-wave approximations, the Hamiltonian of the system is $\hat{H} = \mathcal{N}_{\rm a}\int d^3\mathbf{r}\,\hat{\mathcal{H}}$ ($d^3\mathbf{r} = dxdydz$) with the Hamiltonian density

$$\hat{\mathcal{H}} = -\sum_{\alpha=2}^{3}\hbar\Delta_\alpha \hat{S}_{\alpha\alpha}(\mathbf{r},t) - \hbar\left[\Omega_{\rm p}\hat{S}_{12} + \Omega_{\rm c}\hat{S}_{23} + {\rm h.c.}\right]$$

$$+\mathcal{N}_{\rm a}\int d^3\mathbf{r}'\hat{S}_{33}(\mathbf{r}',t)V_{\rm vdW}(\mathbf{r}'-\mathbf{r})\hat{S}_{33}(\mathbf{r},t),$$

where $\mathcal{N}_{\rm a}$ is the atomic density, Δ_2 and Δ_3 are, respectively, the one- and two-photon detunings; $\hat{S}_{\alpha\beta}\equiv|\beta\rangle\langle\alpha|\exp\{i[(\mathbf{k}_\beta-\mathbf{k}_\alpha)\cdot\mathbf{r}-(\omega_\beta-\omega_\alpha+\Delta_\beta-\Delta_\alpha)t]\}$ is the operator of the atomic transition between $|\alpha\rangle$ and $|\beta\rangle$. Further, $\Omega_{\rm p}=(\mathbf{e}_{\rm p}\cdot\mathbf{p}_{12})\mathcal{E}_{\rm p}/(2\hbar)$ and $\Omega_{\rm c}=(\mathbf{e}_{\rm c}\cdot\mathbf{p}_{23})\mathcal{E}_{\rm c}/(2\hbar)$ represent the half-Rabi frequencies for the probe and control laser fields, respectively, with $\mathbf{p}_{\alpha\beta}$ being the electric-dipole matrix element associated with the transition $|\beta\rangle\leftrightarrow|\alpha\rangle$.

The atomic dynamics is governed by the Heisenberg equations of motion for operators $\hat{S}_{\alpha\beta}(\mathbf{r},t)$, i.e., $i\hbar\partial_t\hat{S}_{\alpha\beta}(\mathbf{r},t)=[\hat{S}_{\alpha\beta}(\mathbf{r},t),\hat{H}]$. Taking the expectation values on both sides of this equation, we obtain the expectation-value equations for the operator, i.e., $\langle\hat{S}_{\alpha\beta}(\mathbf{r},t)\rangle$. To include the decay of the atomic levels due to the spontaneous emission, relaxation constants Γ are introduced [79]. Using the definitions $\rho_{\alpha\beta}(\mathbf{r},t)\equiv\langle\hat{S}_{\alpha\beta}(\mathbf{r},t)\rangle$, the dynamics of the density matrix $\hat{\rho}$ is governed by the Bloch equation,

$$\frac{\partial\hat{\rho}}{\partial t}=-\frac{i}{\hbar}\left[\hat{H},\hat{\rho}\right]+\Gamma\left[\hat{\rho}\right], \tag{1}$$

where $\hat{\rho}(\mathbf{r},t)$ is a 3×3 density matrix, with elements $\rho_{\alpha\beta}$, $\alpha,\beta=1,2,3$, that governs the evolution of the atomic population and coherence. The explicit form of Eq. (1) is presented in Appendix A.

The propagation of the probe field is governed by the Maxwell equation. Under the paraxial and slowly-varying-envelope approximations, it is reduced to

$$i\left(\frac{\partial}{\partial z}+\frac{1}{c}\frac{\partial}{\partial t}\right)\Omega_{\rm p}+\frac{c}{2\omega_p}\nabla_\perp^2\Omega_{\rm p}+\kappa_{12}\rho_{21}=0, \tag{2}$$

where $\nabla_\perp^2=\partial_x^2+\partial_y^2$, and $\kappa_{12}=\mathcal{N}_{\rm a}\omega_p|\mathbf{p}_{12}|^2/(2\varepsilon_0c\hbar)$, with ω_p, ε_0, and c being, respectively, the central frequency of the weak probe laser field, vacuum dielectric constant, and speed of light in vacuum.

B. The nonlocal nonlinear Schrödinger (NNLS) equation

As the probe is much weaker than the control field, the system of the Maxwell-Bloch (MB) equations (1) and (2) can be solved by means of the perturbation theory. Here, we are interested in the steady-state properties of the system, for which the time derivative in the MB equations may be neglected, which is valid for the probe field with a long temporal duration. On the other hand, the Rydberg-Rydberg interaction is treated beyond mean-field approximation [80]. Thus, we solve the MB equations up to the third order with respect to Ω_p. The result is the (2+1)D nonlocal NLS equation for the probe field [22, 80],

$$i\frac{\partial}{\partial z}\Omega_{\rm p}+\frac{c}{2\omega_{\rm p}}\nabla_\perp^2\Omega_{\rm p}+W\left|\Omega_{\rm p}\right|^2\Omega_{\rm p}$$
$$+\int d^2\mathbf{r}'_\perp G(\mathbf{r}_\perp,\mathbf{r}'_\perp)|\Omega_{\rm p}(\mathbf{r}'_\perp,z)|^2\Omega_{\rm p}(\mathbf{r}_\perp,z)=0, \tag{3}$$

with $\mathbf{r}_\perp=(x,y)$ and $d^2\mathbf{r}'_\perp=dx'dy'$. The last two terms in Eq. (3) are contributed by the short-range local and long-range nonlocal optical Kerr nonlinearities, respectively. Explicit expressions of W and G are given in Appendix B.

We convert the propagation equation (3) into a dimensionless form,

$$i\frac{\partial u}{\partial\zeta}+\left(\frac{\partial^2}{\partial\xi^2}+\frac{\partial^2}{\partial\eta^2}\right)u+w|u|^2u$$
$$+u\iint d\xi'd\eta' g(\xi'-\xi,\eta'-\eta)\left|u\left(\xi',\eta'\right)\right|^2=0, \tag{4}$$

where $u=\Omega_{\rm p}/U_0$, $\zeta=z/(2L_{\rm diff})$, $(\xi,\eta)=(x,y)/R_0$, $w=2L_{\rm diff}|U_0|^2W$, and $g(\xi'-\xi,\eta'-\eta)=2L_{\rm diff}R_0^2|U_0|^2G(\xi'-\xi,\eta'-\eta)$, with the diffraction length given by $L_{\rm diff}=\omega_pR_0^2/c$. Here, U_0 and R_0 are typical half-Rabi frequency and beam radius, respectively.

To address a typical example, we refer to ^{88}Sr atoms with atomic levels $|1\rangle=|5s^2\,{}^1S_0\rangle$, $|2\rangle=|5s5p\,{}^1P_1\rangle$, and $|3\rangle=|5sns\,{}^1S_0\rangle$. For the principal quantum number $n=60$, the dispersion parameter is $C_6\approx2\pi\times81.6\,\text{GHz}\,\mu\text{m}^6$ [81, 82]. As $C_6>0$, the Rydberg-Rydberg interaction is attractive, making it possible to support stable bright multi-dimensional solitons [22, 83]. The spontaneous emission decay rates and detunings are, respectively, $\Gamma_{12}\approx2\pi\times32$ MHz, $\Gamma_{23}\approx2\pi\times16.7$ kHz, and $\Delta_2=-2\pi\times240$ MHz , $\Delta_3=2\pi\times0.4$ MHz. The relevant value of the density of the atomic gas is $\mathcal{N}_{\rm a}=2\times10^{11}$ cm^{-3}, and the half-Rabi frequency of the control field is $\Omega_{\rm c}=2\pi\times9$ MHz. The obvious condition, $\Delta_2\gg\Gamma_{12}$, places the system in the dispersive nonlinearity regime, in which the imaginary parts of coefficients in Eq. (3) are much smaller than their real counterparts. Therefore, Eqs. (3) and (4) are written, in the first approximation, with real coefficients [80].

As mentioned above, the exact form of the nonlocal nonlinear response function $g(\xi'-\xi,\eta'-\eta)$ is very cumbersome, it may be represented, with a reasonable accuracy, by a Gaussian [22, 84],

$$g\approx\frac{g_0}{\pi(0.93\sigma)^2}\exp\left[-\frac{(\xi-\xi')^2+(\eta-\eta')^2}{(0.93\sigma)^2}\right], \tag{5}$$

where $g_0=\iint d\xi'd\eta'\,g(\xi'-\xi,\eta'-\eta)$ is a constant, and $\sigma\equiv R_{\rm b}/R_0$ characterizes the nonlocality degree of the nonlinearity, with $R_{\rm b}=(|C_6/\delta_{\rm EIT}|)^{1/6}$ denoting the Rydberg-blockade radius, which is determined by the linewidth of the EIT transmission spectrum (for $|\Delta_2|\gg\Gamma_{12}$), $\delta_{\rm EIT}\approx|\Omega_{\rm c}|^2/|\Delta_2|$. With the parameters adopted above, we get $R_{\rm b}\approx7\,\mu$m.

Since the parameters of the light–atom interaction system are flexible and tunable, the degree of nonlocality σ can be adjusted by tuning the beam waist radius of the laser field R_0 and the Rydberg blockade radius $R_{\rm b}$.

Therefore, by adjusting these parameters, the system can be tuned from local nonlinearity to general nonlocal nonlinearity and strongly nonlocal nonlinearity. According to the degree of the nonlocality, the following analysis is reported in three distinct regimes [80, 85]: (i) the local response, $\sigma \ll 1$; (ii) the nonlocal response, $\sigma \sim 1$; (iii) the strongly nonlocal response, $\sigma \gg 1$.

III. NONLOCAL (2+1)D SMS

A. The binding energy (BE)

To investigate the stability of the SMs, we aim to calculate the BE between N widely separated spatial solitons (i.e., ones involved in the interaction of the *noncontact type*), approximated by the superposition

$$u_m(\xi,\eta) = \sum_{n=1}^{N} u_n(\xi-\xi_n, \eta-\eta_n), \tag{6}$$

composed of N Gaussians, each one, with amplitude A, width a, and chirp (phase-front curvature) b [86], adopted as

$$u_n = A\exp\Big\{-\frac{(\xi-\xi_n)^2+(\eta-\eta_n)^2}{2a^2} + ib(\xi^2+\eta^2) + i[(v_\xi)_n(\xi-\xi_n) + (v_\eta)_n(\eta-\eta_n)] + i\theta_n\Big\}. \tag{7}$$

The phase shift between adjacent solitons is $\theta_{n+1}-\theta_n = \pi$, making the contact interaction between them repulsive, which is necessary for the stability of the appearing SMs [22, 87]. The initial speeds of the soliton cluster (7), set in rotational motion with tangent velocity v, are $\{(v_\xi)_n, (v_\eta)_n\} = v\cdot\{-\eta_n, \xi_n\}$.

The simplest structure under the consideration is a rectangular rhombic SM ($N=4$), which is initially composed of four solitons, placed at positions

$$(\xi_1,\eta_1) = (d_\xi, 0), \quad (\xi_2,\eta_2) = (0, d_\eta),$$
$$(\xi_3,\eta_3) = (-d_\xi, 0), \quad (\xi_4,\eta_4) = (0, -d_\eta), \tag{8}$$

where d_ξ and d_η are the distance from the origin of the coordinate system. A more general SM configuration represents an oblique (compressed) rhombus, with $d_\xi \neq d_\eta$, see Fig. 4 below.

BE is the difference between the SM energy of a molecule [currently represented by ansatz (6)], and the sum of the energies of isolated individual solitons bound in the molecule, i.e., $E_{\rm bind} = E[u_m] - \sum_{n=1}^{N} E[u_n]$ [21]. It is computed as per the energy functional corresponding to Eq. (4):

$$E[u] = \iint d\xi d\eta \left[\left|\frac{\partial u}{\partial \xi}\right|^2 + \left|\frac{\partial u}{\partial \eta}\right|^2 - \frac{w}{2}|u|^4 - \frac{|u|^2}{2}\iint d\xi' d\eta' g(\xi'-\xi, \eta'-\eta)|u|^2\right]. \tag{9}$$

Actually, for the light propagation in the spatial domain, Eq. (9) determines not the physical energy, but rather the total Hamiltonian. The obvious necessary stability condition is the existence of a minimum of $E_{\rm bind}$.

Along with energy (9), the underlying NLS equation (4) conserves the total norm, alias the scaled integral power of the optical beam, $Q = \iint d\xi d\eta\, |u(\xi,\eta)|^2$. Dealing below with rotating modes, it is relevant to consider the angular momentum, which is a dynamical invariant too, $M = i\iint d\xi d\eta u^* (\xi\partial_\eta u - \eta\partial_\xi u)$ [12], where $*$ stands for the complex conjugation.

In the case of weak nonlocal nonlinearity, it can be approximated by the local limit, *viz.*, $g(\xi-\xi', \eta-\eta') \to g_0\delta(\xi-\xi', \eta-\eta')$, with $g_0 = \iint d\xi' d\eta' g(\xi', \eta')$, which converts Eq. (4) into local NLS equation. In Fig. 2(a), the solid line presents the BE as a function the half-size d of the rectangular rhombus (8), with other parameters fixed as $\sigma = 0.1$, $A = 4$, and $a = 1$. In this case, no local minimum of $E_{\rm bind}$ is identified, suggesting that a stable bound state cannot form under the present conditions.

In the limit of strong nonlocality, represented, e.g., by $\sigma = 8$ in Eq. (5), the nonlinear terms in Eq. (4) can be approximated by a quasilinear expression, similar to that in the model of "accessible solitons" [54] $g_1 u + g_2(\xi^2+\eta^2)u$, with constants g_1 and g_2, see Eq. (C2) in Appendix C. In this regime, the BE is plotted vs. d by the dashed line in Fig. 2(a), featuring a shallow minimum, i.e., a possible bound state of the *contact type*, at a small half-size $d \approx 0.61$, the respective separation-to-width ratio being $s \equiv \sqrt{2}d/a \approx 0.86$ [recall the soliton's width a is defined by the Gaussian ansatz (7)]. This result implies that the repulsive force, provided by the out-of-phase setup of the four-soliton chain, is actually too weak to balance the strong effective quadratic potential, $g_2(\xi^2+\eta^2)$, thereby hindering the creation of an SM with a reasonably larger size.

Below, our analysis focuses on large-size SMs achievable when the nonlocality degree σ takes intermediate values. For instance, the previous work [22] has shown that $\sigma = 1.75$ can stabilize the quiescent (non-rotating) rhombic SM. Figure 2(b) illustrates this case, with the inset showing a specific example of the rhombic SM with $A = 4$, $a = 0.95$, $d = 3.87$, $\sigma = 1.75$, and $v = 0$.

B. Rectangular rhombic SMs

We proceed with the search for stable (2+1)D spatial SMs numerically solving Eq. (4) by means of the split-step Fourier method [88]. The initial conditions for the simulations are set to match those presented in Fig. 2(b), with a small random perturbation, represented by factor $[1+\epsilon R(\xi,\eta)]$ multiplying the input. Here, $\epsilon \ll 1$ is the perturbation amplitude, and R is a random variable uniformly distributed in the interval $[-1,+1]$.

Owing to the transverse instability in the case of the nearly local nonlinearity ($\sigma = 0.1$), the multisoliton propagation shown in Fig. 3(a) is highly unstable. This simu-

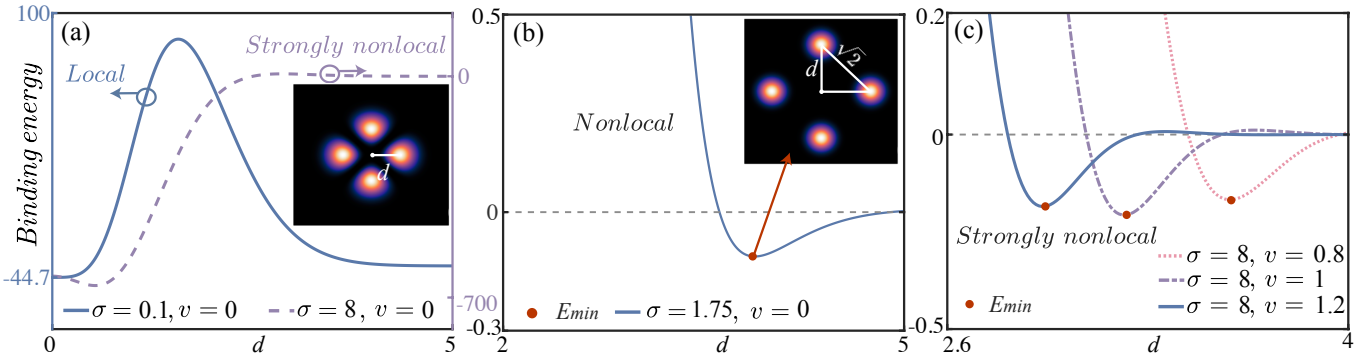


FIG. 2. The binding energy (BE) of the four-soliton rectangular rhombic chain (8). (a) In the case of nearly local nonlinearity [$\sigma = 0.1$ in Eq. (5)], the BE has no minimum, indicating the absence of stable SMs. In the case of strongly nonlocal nonlinearity ($\sigma = 8$), a shallow minimum is observed at $d = 0.61$, suggesting the formation of a small-size non-rotating SM (shown in the inset). The parameters are $A = 4$, $a = 1$, $b = 0$, and $v = 0$. (b) In the regime of moderately nonlocal nonlinearity ($\sigma = 1.75$), a stable non-rotating SM, shown in the inset, is found at $d = 3.87$. The parameters are: $A = 4$, $a = 0.95$, and $v = 0$. (c) In the regime of strongly nonlocal nonlinearity ($\sigma = 8$), varying the initial tangent velocity leads to stable rotating rhombic SMs with different sizes: $d = 3.6$ for $v = 0.8$; $d = 3.23$ for $v = 1$; and $d = 2.94$ for $v = 1.2$. Other parameters are $A = 4$, $a = 1$, and $b = 0$.

lation was initiated by expressions (6), (7), and (8) with parameters $A = 4$, $a = 0.95$, $d_\xi = d_\eta = d = 3.87$, $b = 0$, $Q = 181.4$, and perturbation amplitude $\epsilon = 0.05$.

Shown in Fig. 3(b) is the example of the evolution in the case of moderately nonlocality ($\sigma = 1.75$), with the input taken as per Eq. (8), with $d_\xi = d_\eta = d = 3.87$ and $Q = 181.4$. The rhombic SM is found to be stable, as it relaxes to the self-cleaned form, which remains close to

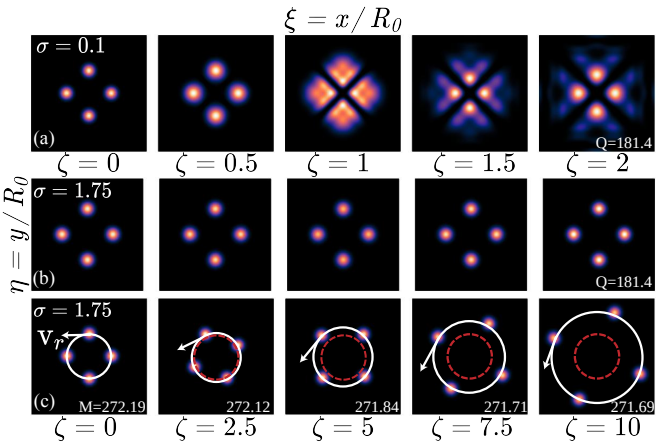


FIG. 3. The simulated evolution of rhombic SMs. The initial conditions are set by Eqs. (6), (7), and (8), with $A = 4$, $a = 0.95$, $d = 3.87$, $b = 0$, and a 5% random perturbation added to the input. (a) In the case of the nearly local nonlinearity, with $\sigma = 0.1$ in Eq. (5), the solitons with power $Q = 181.4$ are unstable. (b) In the case of moderately nonlocal nonlinearity, with $\sigma = 1.75$, the SM with power $Q = 181.4$ is stable. (c) When the rotation, with tangent speed $v = 0.1$, is imposed onto the input, the nonsteadily rotating SM with a gradually increasing size is produced. The red dashed circle shows the initial configuration of the four-soliton molecule; while the radius of the gradually expanding bound state is designated by the white solid curves.

the unperturbed one. A 3D view of the stable propagation is shown in Fig. 1(c). Here, the separation-to-width ratio is $s = \sqrt{2}d/a \approx 5.8$. The appearance of such a stable large-size SM is supported by the giant nonlocal nonlinearity, cf. Ref. [22]. The maximum average power density $P_{\max}$, necessary for the generation of this SM in the experiment, can be obtained from the magnitude of the corresponding Poynting vector [89], which produces an estimate $P_{\max} = 32$ nW. Thus, the power required to generate the stable SMs is found to be in the nanowatt range, which is, roughly, five orders of magnitude smaller than the SM-generation power in fiber-laser systems and optical solid-state waveguides [32, 46, 67, 90].

In Fig. 3(c), the initial rotation with tangent velocity $v = 0.1$ is applied to the soliton chain initially placed along the red dashed circle. As symmetric solitons have tangent velocities of equal magnitude and opposite directions, the overall rotation velocity of the soliton cluster is zero. The rotation gives rise to an outward-directed centrifugal force. As a result, the solitons gradually spiral outward, with their orbital radius, designated by the solid white curve in Fig. 3(c), continuously growing, i.e., a stable rotating SM does not emerge in this case. The initial tangent velocity pushes the solitons in rotation; in the course of the rotation, the angular momentum has values $M = 272.19, 272.12, 271.84, 271.71, 271.69$, corresponding to the propagation distances $\zeta = 0, 2.5, 5, 7.5, 10$.

In addition to the rectangular rhombuses, stable four-soliton molecules can be constructed in the form of non-rotating rhombuses with unequal sizes in the horizontal and vertical directions $d_\xi = 3.5$ and $d_\eta = 4.27$, as shown in Fig. 4(a), for the compression factor $d_\xi/d_\eta \approx 0.819$ and power $Q = 181.4$. On the other hand, Fig. 4(b) shows that a still stronger compression, to $d_\xi/d_\eta \approx 0.738$ with $d_\xi = 3.3$ and $d_\eta = 4.47$, leads to the loss of stability of the oblique rhombus. Thus, there is a stability boundary for the compression factor of the oblique rhom-

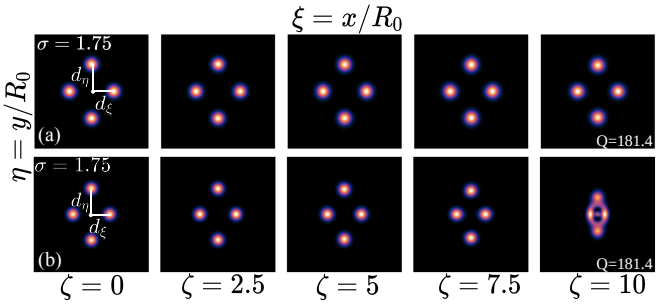


FIG. 4. The simulated evolution of oblique rhombic SMs, with power $Q = 181.4$, and sizes $d_\xi = 3.5$, $d_\eta = 4.27$ the stable SM, (a). With power $Q = 181.4$ and size $d_\xi = 3.3$, $d_\eta = 4.47$ the unstable one, (b). All produced by the system with the moderate nonlocality, $\sigma = 1.75$, and parameters $A = 4$, $a = 0.95$, $b = 0$ in the Gaussian input (7).

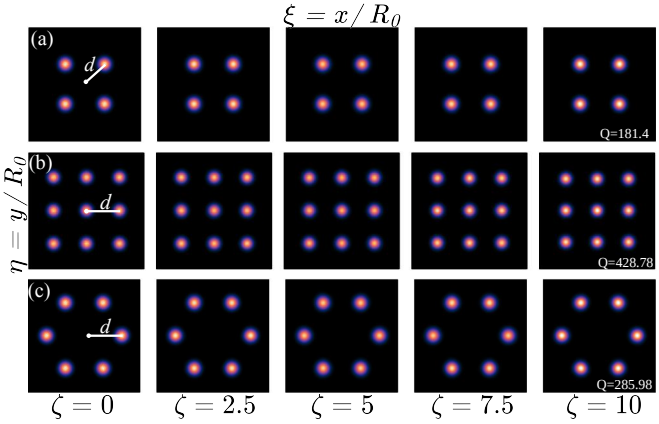


FIG. 5. The evolution of several species of stable SMs in the regime of the moderate strength of the nonlinear nonlocality, with $\sigma = 1.75$. (a) The square-shaped SM with size $d = 3.87$ and power $Q = 181.4$, based on frame (10) . (b) The 3×3 checkerboard-cell SM, with size $d = 5.68$ and power $Q = 428.78$. (c) The hexagonal SM with size $d = 5.57$ and power $Q = 285.98$, based on frame (11). The input parameters in Gaussian (7) are $A = 4$, $a = 0.95$, and $b = 0$.

buses between these two values, for the same moderate nonlocality degree, $\sigma = 1.75$, and the same parameters of Gaussian (7), $A = 4$, $a = 0.95$, $b = 0$, as in Fig. 3(b).

C. Multi-soliton bound states

Parallel to the rhombic SMs, the Rydberg-EIT system supports other species of multi-soliton molecules. As the starting point for producing additional species, one can rotate a rectangular rhombus by 45 degrees and consider it as a square-shaped SM, with the individual solitons set at position

$$(\xi, \eta) = (\pm\sqrt{2}d/2, \pm\sqrt{2}d/2). \tag{10}$$

For the same value $d = 3.87$ and $\sigma = 1.75$, as adopted above for the moderate degree of the nonlocality in Fig. 3(b), Fig. 5(a) demonstrates the stable propagation of the square-shaped SM, with parameters of Gaussian (7) taken as $A = 4$, $a = 0.95$, $b = 0$, and $Q = 181.4$. This result is similar to the stability of the rectangular rhombus in Fig. 3(b).

Proceeding from the square cell in Fig. 5(a), it is possible to produce a new stable SM structure, in the form of a checkerboard cell, composed of 9 solitons, which is displayed in Fig. 5(b). The consideration of the corresponding BE produces the equilibrium value, $d = 5.68$, for the same input parameters as in Fig. 5(a).

A stable SM shaped as a hexagonal cell can be constructed too, as shown in Fig. 5(c). In this configuration, the constituent solitons are set as points

$$(\xi_n, \eta_n) = d[\cos(n\pi/3), \sin(n\pi/3)], \; n = 1, 2, 3, 4, 5, 6, \tag{11}$$

and the equilibrium value of the separation, corresponding to the minimum of the BE, is $d = 5.57$, for the same set of parameters in the input Gaussian as used above, *viz.*, $A = 4$, $a = 0.95$, $b = 0$, and $Q = 285.98$. Thus, we conclude that the Rydberg-EIT system sustains a variety of stable SM configurations, including rectangular and oblique rhombic, square-shaped, checkerboard-cell, and hexagonal ones.

IV. ROTATING SMS AND BMS (BREATHER MOLECULES) IN THE REGIME OF STRONGLY NONLOCAL NONLINEARITY

A. The effective propagation equation and BE

We now proceed to the strongly nonlocal regime. Compared to the intensity profile of the probe field, the response function G in Eq. (3) is very flat in a vicinity of $\mathrm{r}'_\perp = \mathrm{r}_\perp$, allowing to use its Taylor expansion, $G(\mathrm{r}'_\perp - \mathrm{r}_\perp) \approx G(0) + G''(0)r_\perp^2/2$ [54, 80]. In this case, the nonlocal term in Eq. (4) can be reduced to a quasi-linear form, including the usual 2D harmonic-oscillator potential, so that the simplified equation becomes

$$i\frac{\partial \Phi}{\partial \zeta} + \left(\frac{\partial^2}{\partial \xi^2} + \frac{\partial^2}{\partial \eta^2}\right)\Phi + w|\Phi|^2\Phi + g_2(\xi^2+\eta^2)\Phi = 0. \tag{12}$$

where $\Phi \equiv u(\xi, \eta, \zeta)\exp(ig_1\zeta)$ and $g_1 \equiv 2L_{\rm diff}P_0G(0)$, $g_2 \equiv L_{\rm diff}R_0^2P_0G''(0)$. This reduced equation admits an approximate analytical Gaussian-shaped SM solution, see Appendix D.

To study SMs in the strongly nonlocal regime, we refer to a relevant set of physical parameters: $\Omega_{\rm c} = 2\pi \times 25$ MHz, $\Delta_2 = -2\pi \times 260$ MHz, $\Delta_3 = 2\pi \times 13$ MHz, $R_0 = 2.2\,\mu$m, $\mathcal{N}_{\rm a} = 5.8 \times 10^{12}$ cm^{-3}, and $C_6 \approx 2\pi \times 167\,\mathrm{THz} \cdot \mu\mathrm{m}^6$, with the principal quantum number $n = 120$. For these parameters, the radius of the Rydberg blockade is $R_b = 18\,\mu$m, and the nonlocality degree is indeed large, $\sigma =$

$R_b/R_0 \approx 8$, the other parameters in Eq. (12) being $w = 0.02$ and $g_2 = -1$.

The expression for the energy functional corresponding to Eq. (12)

$$E[\Phi] = \iint d\xi d\eta \left[\left| \frac{\partial \Phi}{\partial \xi} \right|^2 + \left| \frac{\partial \Phi}{\partial \eta} \right|^2 - \frac{w}{2}|\Phi|^4 - \frac{g_2}{2}(\xi^2 + \eta^2)|\Phi|^2 \right]. \quad (13)$$

Analyzing the BE corresponding to the energy functional (13), we find that non-rotating N-soliton clusters cannot form large stable SMs in the strongly nonlocal regime, as shown in Fig. 2(a) for $N = 4$ and is also valid for larger values of N. The analytical result shown in Appendix D clarify this conclusion: Eqs. (D2a) and (D2b) with $\mathbf{v}_r = ((v_\xi)_n, (v_\eta)_n) = 0$ predict periodic oscillations of the center-of-mass of each soliton $[\xi_n(\zeta), \eta_n(\zeta)] = [\xi_n(0)\cos\alpha, \eta_n(0)\cos\alpha]$, preventing the formation of a stationary SM. An alternative possibility to construct SMs under strong nonlocality is to use the rotation imposed onto the initial cluster. The respective BE plot in Fig. 9(a) reveals more than one equilibrium point. When the soliton is placed at the first equilibrium position, the resulting structure is a contact-type SM, as shown in Fig. 9(c); details are provided in Appendix E. In this work, however, we focus on long-range, non-contact SMs, therefore only the second equilibrium position is considered in Fig. 2(c).

As seen in Fig. 2(c) for $\sigma = 8$, varying the initial rotation velocity easily produces large-size SMs. This is possible because the rotation induces a centrifugal force, enabling the attractive and repulsive forces to balance each other, and thus form stable SMs. When the initial velocity is large, the corresponding centrifugal force is strong, making the separation between the constituent solitons smaller, helping to generate a stronger attractive force that balances the repulsive centrifugal one. For example, at $v = 1.2$, the equilibrium position is $d = 2.94$, see the blue solid line in Fig. 2(c). On the other hand, when the initial velocity is small and the corresponding centrifugal force is weak, hence the equilibrium separation between the bound solitons increases, reducing the attractive force. In particular, at $v = 0.8$, the equilibrium position is $d = 3.6$, see the red dashed line in Fig. 2(c). The parameters of the Gaussian (7) in this case are the same as above, i.e., $A = 4$, $a = 1$, and $b = 0$.

B. Rotating SMs and BMs

Based on the approximate ansatz for the SM solution for far separated solitons, $\Psi_N(\mathbf{r}, \zeta) = \sum_{n=1}^{N} \Phi_n(\mathbf{r}, \zeta)$ (explicit expressions for $\Phi_n(\mathbf{r}, \zeta)$ are given in Appendix D), we derive the centroid equation of motion for the individual solitons, i.e., $v^2\xi_n^2 + \eta_n^2 = v^2 d^2$, which are actually determined by the Ehrenfest theorem [91], see details in Appendix E. When $v = 1$, it reduces to the circle equation: $\xi_1^2 + \eta_1^2 = d^2$, with the circle's radius exactly equal to that of the initial ring. Therefore, every constituent Gaussian soliton follows a concentric circular trajectory. When $v \neq 1$, the centroid equation of motion reduces to one for the ellipse. Based on the latter equation, we can define the eccentricity, which is $e = \sqrt{1 - v^2}$ for $0 < v < 1$, and $e = \sqrt{1 - 1/v^2}$ for $v > 1$.

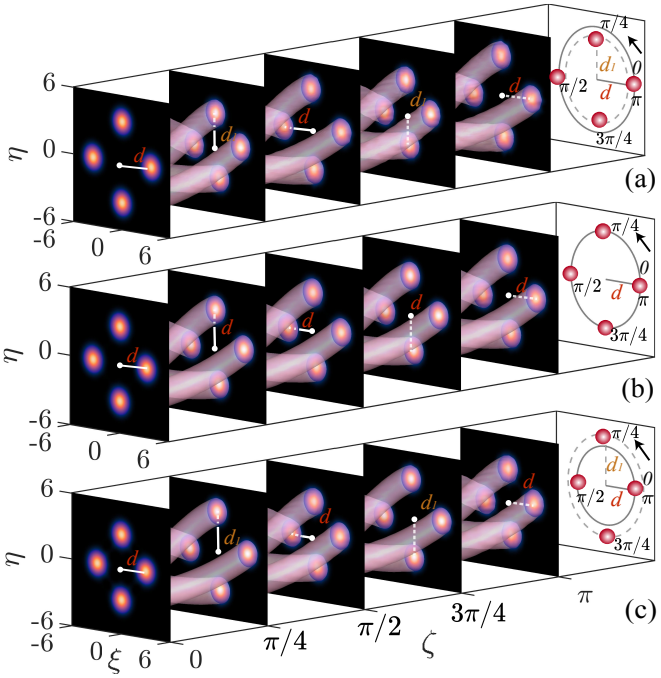


FIG. 6. The evolution of rhombic SMs and BMs. (a) During the propagation, the SM first executes a centripetal motion until it attains an extremum, then switches to centrifugal motion until it returns to the initial radius, with initial velocity $v = 0.8$. This breathing mode repeats with the period of $\pi/2$. Simultaneously, the BM rotates, completing one full turn with period π. As the initial rotation velocity is directed counterclockwise, the BM rotates counter-clockwise too (as shown by black arrows), with period π. (b) With the initial rotation velocity $v = 1$, the SM exhibits counter-clockwise rotational motion. The radius of the rotation circle is exactly that of the initial ring. (c) The same as (a), but for $v = 1.2$. The SM first executes centrifugal motion until it attains the maximum, then switches to centripetal motion until returns to the initial radius. The rotation and breathing periods are the same as those in panel (a). In the (ξ, η) cross-sections, d and d_1 represent the radius at the corresponding propagation distance ζ. In the last cross-section, the solid circle marks the initial radial position of the solitons (d); the dashed circle indicates the extremal radial position reached during the breathing cycle (d_1). The four circles mark the spatial positions of the first soliton at $\zeta = 0$, $\pi/4$, $\pi/2$, and $3\pi/4$, respectively. At $\zeta = \pi$, the first soliton returns to its initial position. Other parameters are the same as in Fig. 2(c).

In Fig. 6(a), initial rotation velocity $v = 0.8$ is applied to the SMs. In the course of the propagation, the constituent solitons spiral inward, their orbital radius contin-

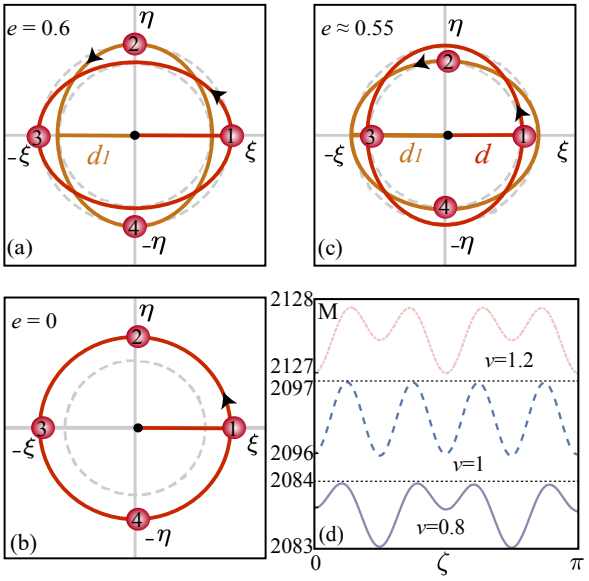


FIG. 7. Panel (a), (b), and (c) display the trajectories corresponding to Figs. 6(a), (b), and (c), respectively: (a) and (c) are ellipses with eccentricities 0.6 ($v = 0.8$) and 0.55 ($v = 1.2$), while (b) is a circle ($e = 0$, $v = 1$). Panel (d) displays the evolution of the angular momentum corresponding to (a) $v = 0.8$ [purple solid line], (b) $v = 1$ [blue dashed line], and $v = 1.2$ [red dash-dotted line].

uously decreasing until it attains a minimum at $\zeta = \pi/4$. In contrast, in the interval $\pi/4 < \zeta < \pi/2$, the solitons spiral outward, while their orbital radius grows until $\zeta = \pi/2$, where it returns to the initial value. In the propagation diagram (the first and third cross sections), we observe that a single soliton has performed half a period of the rotation during this propagation interval. The motion then repeats the original sequence from 0 to $\pi/2$, giving the breathing oscillations a period of $\pi/2$. We therefore refer to these bound states as BMs ("breather molecules") [48, 92, 93].

The breathing period can be obtained, from the equation of motion for the first soliton in the SM, i.e., $v^2\xi_1^2 + \eta_1^2 = v^2 d^2$. It shows that distance d from the center of mass of the first soliton, (ξ_1, η_1), to the origin of the coordinate system varies as $d \propto |\cos(\beta_0\zeta)|, |\sin(\beta_0\zeta)|$. Here, β_0 is the propagation constant, determined by the system's parameters, such as atomic density, detunings, and the strength of the Rydberg interaction. The system's parameters given above yield $\beta_0 = 2$. In this case, the breathing oscillation period of the single soliton is $T_b = \pi/\beta_0 = \pi/2$. By choosing different values of the system parameters, one can change the propagation constant β_0 and the respective breathing period. Thus, our study suggests a scheme for manipulating the breathing period of the BM.

The last cross-section in Fig. 6(a) shows the trajectory of the first soliton. We find that, when $\zeta = \pi$, the first soliton returns to its original position, indicating that the rotation period is π, and Fig. 7(a) presents the corresponding trajectories of four solitons from Fig. 6(a). The red and yellow ellipses with eccentricity $e = 0.6$ denote, severally, the trajectories of the first and third solitons, and of the second and fourth ones. The rotation period can likewise be obtained from the analytical results. The equations of motion for the center of mass of each individual soliton in the SM in produced in Appendix D, see Eqs. (D2a) and (D2b). These equations show that the center-of-mass coordinates (ξ_n, η_n) of the n-th soliton vary sinusoidally as the function of the propagation distance ζ, i.e., $\xi_n(\eta_n) \propto [\cos(\beta_0\zeta), \sin(\beta_0\zeta)]$. Consequently, the SM rotation period is $T_r = 2\pi/\beta_0 = \pi$. The propagation constant β_0 can be adjusted by tuning the system's parameters, thereby enabling control over the rotation period.

When $v = 1$, the SM exhibits no radial motion (neither centripetal nor centrifugal), simply rotating along its initial orbit, and the rotation period is π, see Fig. 6(b). Moreover, the projected SM trajectory remains on the circle at all times shown in the last cross-section in Fig. 6(b). Figure 7(b) shows the trajectory of four solitons corresponding to Fig. 6(b), which is a circle with eccentricity $e = 0$.

As shown in Fig. 6(c), with initial rotation velocity $v = 1.2$, the SMs spiral outward, their orbital radius increasing until it reaches a maximum at $\zeta = \pi/4$. Subsequently, in the interval $\pi/4 < \zeta < \pi/2$, the SMs spiral inward, their orbital radius decreasing until $\zeta = \pi/2$, where it returns to the initial radius. The motion then repeats itself, giving the breathing period of $\pi/2$. Figure 7(c) shows that the trajectory of the four solitons corresponding to Fig. 6(c) is an ellipse with eccentricity $e \approx 0.55$. Thus, adjusting the initial rotation velocity, one can not only control the trajectories of SMs and BMs, but also perform mutual conversion between them.

The initial tangent velocity gives rise to rotation of the SM, the respective angular momentum M being determined by the magnitude of the initial tangent velocity. Figure 7(d) shows the variation of M in the course of the propagation, for different initial tangent velocities. Here, purple solid, blue dashed, and red dash-dotted lines correspond to initial tangent velocities $v = 0.8$, 1, and 1.2, respectively.

To further verify the SM and BM trajectories, we analyzed equations of motion for individual solitons. We find that, when $v = 0.8$, distance d from the soliton to the origin undergoes periodic variations, first decreasing and then increasing, see Fig. 8(a), the ξ_1 and η_1 coordinates of the soliton's center of mass oscillating as cosine and sine, respectively. These results are consistent with those displayed in Fig. 6(a). Concerning Fig. 6(b), with the initial rotation velocity $v = 1$, we have found that the soliton's distance from the origin remains fixed on the circle, with its center-of-mass coordinates ξ_1 and η_1 oscillating as cosine and sine, respectively, indicating that the soliton simply rotates along its initial orbit, with period π, see Fig. 8(b). This result is consistent with Fig. 6(b) and the analytical result presented in Appendix D, see

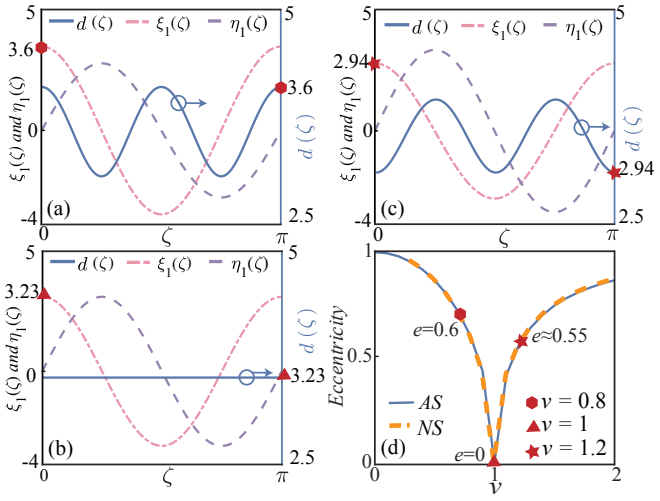


FIG. 8. Trajectory projection and eccentricity. (a), (b), and (c) correspond to the trajectory projections of the single soliton located at $(\xi_1, \eta_1) = (d, 0)$ under three different velocities $v = 0.8$, 1, 1.2 shown in Fig. 6. The solid lines depict the evolution of the center-of-mass distance of first soliton; the red dotted-dashed and purple dashed lines illustrate the trajectory projections of the ξ_1- and η_1-coordinates. The marked points indicate the initial positions and $\zeta = \pi$. (d) Displays the dependence of eccentricity on velocity v. The solid line represents the analytical solution (AS), while the dotted line corresponds to numerical simulation (NS). In panel (d), the three marks correspond to the eccentricities of the trajectories in panels (a), (b), and (c), respectively.

Eqs. (D2a) and (D2b). When $v = 1.2$, distance d from the soliton to the origin undergoes periodic variations, first increasing and then decreasing. Meanwhile, the ξ_1 and η_1 coordinates of the soliton's center-of-mass oscillate as cosine and sine, see Fig. 8(c).

Figure 8(d) displays the relation between the eccentricity and rotation velocity. The solid line represents the analytically derived variation of the eccentricity, while the dashed line represents the respective numerical results, showing good agreement between both [94]. The three markers correspond to Figs. 8(a), (b), and (c), with eccentricities $e = 0.6$, 0, and 0.55, respectively. No numerical data are presented in the range of $0 < v < 0.3$ due to the absence of a local BE minimum, indicating that there are no stable SMs or BMs in this velocity range.

V. CONCLUSION

Numerous experimental observations of SMs have been reported in ultrafast fiber lasers operating in the mode-locking regime [16, 17, 24, 30, 45–47, 92, 93, 95]. Naturally, fiber systems support SMs solely in the 1D form. In this work, we elaborate the scheme the creation of effectively (2+1)D SMs in ultracold Rydberg atomic gases. To construct SMs, the first step is to create multi-soliton clusters. To this end, one can use a phase-imprinting technique, in which the laser beam is transmitted through an appropriately oriented set of microscopic glass slides (a phase mask) [96]. A four-soliton cluster can be created by means of two perpendicularly oriented glass slides, with an appropriate tilt inducing a π shift between adjacent solitons. Subsequently, the four-soliton structure with random noise is transmitted to the input face of the atomic cell. Under the action of the long-range nonlocal Rydberg interactions, multiple solitons are locked at a specific equilibrium positions, forming stable SMs.

In summary, we have proposed a theoretical scheme for realizing SMs and BMs in the ultracold Rydberg atomic gas with EIT. In this system, the interplay between EIT and strong long-range Rydberg interactions generates the well-defined nonlocal Kerr nonlinearity, which secures the stability of the (2+1)-dimensional SMs, that is not possible in the case of the local nonlinearity. In the system with the moderate degree of the nonlocality, we have predicted various species of stable non-rotating SMs, including rectangular and oblique rhombuses, checkerboard cells, and hexagons. In the regime of strong nonlocality, the introduction of rotation is necessary, to secure to balance of the strong attraction with the centrifugal force. Varying the rotation velocity, periodic centrifugal-centripetal "breathing" dynamics of the solitons is maintained, leading to the creation of BMs. The present results reveal the crucial roles of the nonlocality and rotation in the formation of SMs and BMs, providing a reliable means for controlling the size, rotation, and breathing dynamics of these multi-soliton bound states. The so engineered robust bound complexes of optical solitons can find applications in the design of photonic data-processing and transmission technologies.

As an extension of the analysis, it may be interesting to construct bound states of several optical solitons with *intrinsic vorticity*. In particular, it may be possible to set such self-supported complexes of vortex solitons in overall rotation, thus realizing the concept of "supervortices", cf. Ref. [97].

ACKNOWLEDGMENTS

L.Q., Y.Z., and S.Z. acknowledge the support of National Natural Science Foundation of China (Grant No. 12404377, No. 12304357, and No. 62505079). X.Z. acknowledges the support from the Key Scientific Research Project of Colleges and Universities in Henan Province (Grant No. 26B140007) and Natural Science Foundation of Henan Province (Grant No. 252300421995). Z.Z acknowledges the support from the Key International Cooperation Project in Henan Province (Grant No. 261111521200).

Appendix A: The Bloch equations

The full system of the optical Bloch equations for the evolution of the density-matrix elements $\rho_{\alpha\beta} \equiv \langle \hat{S}_{\beta\alpha} \rangle$ is

$$i\frac{\partial}{\partial t}\rho_{11} - i\Gamma_{12}\rho_{22} + \Omega_p^*\rho_{21} - \Omega_p\rho_{12} = 0, \tag{A1a}$$

$$i\frac{\partial}{\partial t}\rho_{22} + i\Gamma_{12}\rho_{22} - i\Gamma_{23}\rho_{33} + \Omega_c^*\rho_{32} - \Omega_c\rho_{23} - \Omega_p^*\rho_{21} + \Omega_p\rho_{12} = 0, \tag{A1b}$$

$$i\frac{\partial}{\partial t}\rho_{33} + i\Gamma_{23}\rho_{33} - \Omega_c^*\rho_{32} + \Omega_c\rho_{23} = 0, \tag{A1c}$$

$$\left(i\frac{\partial}{\partial t} + d_{21}\right)\rho_{21} + \Omega_c^*\rho_{31} - \Omega_p(\rho_{22} - \rho_{11}) = 0, \tag{A1d}$$

$$\left(i\frac{\partial}{\partial t} + d_{31}\right)\rho_{31} - \Omega_p\rho_{32} + \Omega_c\rho_{21} - \frac{\mathcal{N}_a}{2}\int d^3\mathbf{r}' V(\mathbf{r}' - \mathbf{r})\rho\rho_{33,31}(\mathbf{r}', \mathbf{r}, t) = 0, \tag{A1e}$$

$$\left(i\frac{\partial}{\partial t} + d_{32}\right)\rho_{32} - \Omega_p^*\rho_{31} - \Omega_c(\rho_{33} - \rho_{22}) - \frac{\mathcal{N}_a}{2}\int d^3\mathbf{r}' V(\mathbf{r}' - \mathbf{r})\rho\rho_{33,32}(\mathbf{r}', \mathbf{r}, t) = 0, \tag{A1f}$$

where $\rho_{\alpha\beta} = \langle \hat{S}_{\beta\alpha} \rangle$ are one-body density matrix elements, $d_{\alpha\beta} = \Delta_\beta - \Delta_\alpha + i\gamma_{\alpha\beta}$ ($\Delta_1 = 0$), $\gamma_{\alpha\beta} = (\Gamma_\alpha + \Gamma_\beta)/2 + \gamma_{\alpha\beta}^{\rm dep}$ ($\alpha \neq \beta$), and $\Gamma_\beta = \sum_{\alpha<\beta}\Gamma_{\alpha\beta}$, with $\Gamma_{\alpha\beta}$ and $\gamma_{\alpha\beta}^{\rm dep}$ being the spontaneous decay and dephasing rates, respectively, for the $|\beta\rangle \to |\alpha\rangle$ transition.

In the last term on left-hand side of Eqs. (A1e) and (A1f), the two-body correlators $\rho_{33,3\alpha}(\mathbf{r}', \mathbf{r}, t) \equiv \langle \hat{S}_{33}(\mathbf{r}', t)\hat{S}_{3\alpha}(\mathbf{r}, t)\rangle$ ($\alpha = 1, 2$) originate from the Rydberg-Rydberg interaction.

Appendix B: The solution of the Bloch equations

We assume that the probe field is much weaker than the control field and atoms initially populate state $|1\rangle$. Thus, one can use the asymptotic expansion for the density matrix: $\rho_{\alpha\beta} = \epsilon\rho_{\alpha\beta}^{(1)} + \epsilon^2\rho_{\alpha\beta}^{(2)} + \epsilon^3\rho_{\alpha\beta}^{(3)}\cdots$ ($\alpha, \beta = 1, 2, 3$), $\Omega_p = \sum_{l=1}\epsilon^l\Omega_p^{(l)}$, where ϵ a parameter characterizing the amplitude of Ω_p. The terms of the expansion are considered as functions of multiscale variables, $z_l = \epsilon^l z$ ($l = 0, 1, 2$), and $(x_1, y_1) = \epsilon(x, y)$. Substituting the expansion in the MB equations, and comparing coefficients in front of ϵ^l ($l = 1, 2, \cdots$), we obtain a set of linear inhomogeneous equations which can be solved order by order. Notice that in this work we are interested in the steady-state properties of the system, for which the time derivative in the MB equations may be neglected, which is valid for the probe field with a long temporal duration.

At the first order ($l = 1$), we obtain the solution

$$\rho_{21}^{(1)} = \frac{d_{31}}{D_1},\ \rho_{31}^{(1)} = -\frac{\Omega_c}{D_1},$$

where $D_1 = |\Omega_c|^2 - d_{21}d_{31}$.

For the second order ($l = 2$), one obtains the solution

$$\rho_{11}^{(2)} = \frac{[i\Gamma_{23} - 2|\Omega_c|^2M_1]M_2 - i\Gamma_{12}|\Omega_c|^2M_3}{\Gamma_{12}\Gamma_{23} - i\Gamma_{12}|\Omega_c|^2M_1}, \tag{B2a}$$

$$\rho_{33}^{(2)} = \frac{1}{i\Gamma_{12}}\left(M_2 - i\Gamma_{12}\rho_{11}^{(2)}\right), \tag{B2b}$$

$$\rho_{32}^{(2)} = \frac{1}{d_{32}}\left(-\frac{\Omega_c}{D_1} + 2\Omega_c\rho_{33}^{(2)} + \Omega_c\rho_{11}^{(2)}\right), \tag{B2c}$$

where $M_1 = 1/d_{32} - 1/d_{32}^*$, $M_2 = d_{31}^*/D_1^* - d_{31}/D_1$, and $M_3 = 1/(D_1^*d_{32}^*) - 1/(D_1d_{32})$.

At the third order ($l = 3$), the solution reads

$$\rho_{21}^{(3)} = \mathcal{A}_{21}^{(3)} + \mathcal{N}_a\mathcal{B}_{21}^{(3)}, \tag{B3a}$$

$$\rho_{31}^{(3)} = \mathcal{A}_{31}^{(3)} + \mathcal{N}_a\mathcal{B}_{31}^{(3)}, \tag{B3b}$$

with

$$\mathcal{A}_{21}^{(3)} = \frac{\Omega_c^*\rho_{32}^{(2)} + d_{31}(2\rho_{11}^{(2)} + \rho_{33}^{(2)})}{D_1}, \tag{B4a}$$

$$\mathcal{B}_{21}^{(3)} = \frac{\Omega_c^*\int d^3\mathbf{r}'\rho_{33,31}^{(3)}(\mathbf{r}' - \mathbf{r})V(\mathbf{r}' - \mathbf{r})}{D_1}, \tag{B4b}$$

$$\mathcal{A}_{31}^{(3)} = \frac{-(2\rho_{11}^{(2)} + \rho_{33}^{(2)})\Omega_c + d_{21}\rho_{32}^{(2)}}{D_1}, \tag{B4c}$$

$$\mathcal{B}_{31}^{(3)} = \frac{\int d^3\mathbf{r}'\rho_{33,31}^{(3)}(\mathbf{r}' - \mathbf{r})V(\mathbf{r}' - \mathbf{r})d_{21}}{D_1}, \tag{B4d}$$

where $\rho_{33,31}^{(3)}(\mathbf{r}' - \mathbf{r}) = \langle \hat{S}_{33}(\mathbf{r}')\hat{S}_{31}(\mathbf{r})\rangle$ is the two-body correlator.

According to the third-order solution, expressions for coefficients of the local and nonlocal optical Kerr nonlinearity are

$$W = \kappa_{12}\mathcal{A}_{21}^{(3)}, \tag{B5a}$$

$$G = \kappa_{12}\mathcal{N}_a\mathcal{B}_{21}^{(3)}. \tag{B5b}$$

Because the dephasing in the system is much weaker than the spontaneous emission, Eq. (B5b) can be approximately written as [22, 80]

$$G \approx \kappa_{12}\mathcal{N}_a\frac{2(d_{21} + d_{31})|\Omega_c|^4/|D_1|^2}{D_1D_2[2d_{31} - V(\mathbf{r}' - \mathbf{r})] - 2d_{21}|\Omega_c|^2},$$

with $D_2 = |\Omega_c|^2 - d_{21}(d_{21} + d_{31})$.

Appendix C: The NLS equation in the regime of strongly nonlocal nonlinearity

Assuming that the pulse's temporal duration is sufficiently long to make the group-velocity dispersion of the system negligible, the light propagation in the spatial domain is governed by Eq. (3). In the case of strong nonlocality, the response function G in Eq. (3) is very flat

near $(x', y') = (x, y)$, in comparison to the intensity profile of the probe field, which allows one to use the Taylor's expansion, $G(x - x', y - y') \approx G(0) + G''(0)(x^2 + y^2)/2$ [54, 80]. In this case, Eq. (3) can be written as

$$i\frac{\partial}{\partial z}\Omega_{\rm p}+\frac{c}{2\omega_{\rm p}}\nabla_{\perp}^2\Omega_{\rm p}+W|\Omega_{\rm p}|^2\Omega_{\rm p} +P_0[G(0)+\frac{1}{2}G''(0)(x^2+y^2)]\Omega_{\rm p}=0, \quad \text{(C1)}$$

where $P_0 = \iint dx\, dy\, |\Omega_{\rm p}|^2$ is the power of the probe field. Because the expression for the nonlocal response function $G(x - x', y - y')$ is very complex, the coefficients $G(0)$ and $G_2''(0)$ were obtained in the numerical form. Equation (C1) can be cast in the scaled form,

$$i\frac{\partial u}{\partial \zeta}+\left(\frac{\partial^2}{\partial \xi^2}+\frac{\partial^2}{\partial \eta^2}\right)u+w|u|^2u+g_1u+g_2(\xi^2+\eta^2)u=0, \quad \text{(C2)}$$

where $w = 2W|u_0|^2 L_{\rm diff}$, $g_1 = 2L_{\rm diff}P_0G(0)$, $g_2 = L_{\rm diff}R_0^2P_0G''(0)$. Thus, in the case of the strongly nonlocal nonlinear response region, the nonlocal part of the governing NLS equation (C2) amounts to the quasi-linear form with the harmonic-oscillator potential, similar to the model of "accessible soliton" [54]. By substituting $\Phi = u\exp(ig_1\zeta)$, Eq. (C2) is further reduced to Eq. (12) in the main text, which makes it possible to look for solutions in the form of Gaussians (approximate ones, if Eq. (C2) keeps $w \neq 0$) [54, 98].

Appendix D: The analytical solution for SMs

In the strongly nonlocal regime, Eq. (12) with $w = 0$ has an exact Gaussian solution [94], which is actually tantamount to the well known exact solution of the Schrödinger equation, representing a wave function of the harmonic oscillator in quantum mechanics [91]

$$\Phi(\mathbf{r},\zeta)=A\exp\left[-\frac{\xi^2+\eta^2}{2a^2(\zeta)}+ib(\zeta)\left(\xi^2+\eta^2\right)+i\theta(\zeta)\right],$$

where

$$a(\zeta)=a_0\left(\cos^2\alpha+P_r\sin^2\alpha\right)^{1/2},$$
$$b(\zeta)=\frac{\beta_0(P_r-1)\sin(2\alpha)}{4\left(\cos^2\alpha+P_r\sin^2\alpha\right)},$$
$$\theta(\zeta)=-\arctan\left(\sqrt{P_r}\tan\alpha\right),$$

denote the beam's width, phase-front curvature (chirp) [86], and overall phase, respectively. Further, $a_0 = a(0)$ is the initial width of the beam, and $\alpha = \beta_0\zeta$, where $\beta_0 = 2\sqrt{|L_{\rm diff}R_0^2P_0G''(0)|}$ is the propagation constant. We define $P_r = P_c/P_0$ as the power ratio, $P_c = 1/|L_{\rm diff}R_0^2G''(0)a^4|$ being the critical power. When $P_r = 1$ ($P_0 = P_c$), the chirp-induced compression exactly balances the diffraction, hence the respective Gaussian beam preserves its width in the course of the propagation, being tantamount to the ground-state wave function of the 2D harmonic oscillator in quantum mechanics. With $P_r \neq 1$, the width of the Gaussian beam periodically oscillates, making it possible to identify it as quasi-linear breather [54, 98]. We primarily focus on the case $P_0 = P_c$, when the beam keep its steady state.

If $\Phi(\mathbf{r}, \zeta)$ is a solution of Eq. (12), then

$$\Phi_n(\mathbf{r},\zeta)=\Phi(\mathbf{r}-\mathbf{r}_n(\zeta),\zeta)\exp\left[i\mathbf{v}_r(\zeta)(\mathbf{r}-\mathbf{r}_n(\zeta))+i\Theta(\zeta)\right]$$

are solutions as well, where $\mathbf{r}_n(\zeta)$, $\mathbf{v}_r(\zeta)$, $\Theta(\zeta)$ satisfy the following equations:

$$\mathbf{r}_n''(\zeta)+\beta_0^2\mathbf{r}_n(\zeta)=0,$$
$$\mathbf{v}_r(\zeta)=\frac{1}{2}\mathbf{r}_n'(\zeta),$$
$$\Theta'(\zeta)=\frac{1}{4}\left[\beta_0^2\mathbf{r}_n^2(\zeta)-\mathbf{r}_n'^2(\zeta)\right].$$

For the quasi-linear equation (C2), we construct a coherent superposition of N Gaussian beams, the respective quasi-linear limit form of the SM being

$$\Psi_N(\mathbf{r},\zeta)=\sum_{n=1}^{N}\Phi_n(\mathbf{r},\zeta). \quad \text{(D1)}$$

Explicit expressions for $\Phi_n(\mathbf{r}, \zeta)$ can be written in

$$\Phi_n(\mathbf{r},\zeta)=A\exp\Big\{-\frac{(\xi-\xi_n)^2+(\eta-\eta_n)^2}{2a^2(\zeta)}+ib(\zeta)\left[(\xi-\xi_n)^2+(\eta-\eta_n)^2\right]+i[(v_\xi)_n(\xi-\xi_n)+(v_\eta)_n(\eta-\eta_n)]+i\Theta_n(\zeta)+i\theta_n\Big\},$$

where

$$\xi_n(\zeta)=\xi_n(0)\cos\alpha+\frac{(v_\xi)_n(0)}{\beta_0}\sin\alpha, \quad \text{(D2a)}$$
$$\eta_n(\zeta)=\eta_n(0)\cos\alpha+\frac{(v_\eta)_n(0)}{\beta_0}\sin\alpha, \quad \text{(D2b)}$$
$$(v_\xi)_n(\zeta)=-\frac{1}{2}\xi_n(0)\beta_0\sin\alpha+\frac{1}{2}(v_\xi)_n(0)\cos\alpha, \quad \text{(D2c)}$$
$$(v_\eta)_n(\zeta)=-\frac{1}{2}\eta_n(0)\beta_0\sin\alpha+\frac{1}{2}(v_\eta)_n(0)\cos\alpha, \quad \text{(D2d)}$$
$$\Theta_n(\zeta)=\frac{1}{8}\left[\beta_0\left(\xi_n^2(0)+\eta_n^2(0)\right)-\frac{(v_\xi)_n^2(0)+(v_\eta)_n^2(0)}{\beta_0}\right]\times\sin(2\alpha)-\frac{1}{4}\left[\xi_n(0)(v_\xi)_n(0)+\eta_n(0)(v_\eta)_n(0)\right]\cos(2\alpha). \quad \text{(D2e)}$$

The initial rotation velocity of the SM is defined as $[(v_\xi)_n(0), (v_\eta)_n(0)] = v\beta_0[-\eta_n(0), \xi_n(0)]$. The initial rotation velocity of each Gaussian constituent is determined by the condition of obliquely symmetric incidence, i.e., by angle ϑ between the wave vector and the propagation direction at the incidence position [98]. The wave vector of each constituent at $\zeta = 0$ can be written as

$$\mathbf{k}_n = k_{n\xi}\mathbf{e}_\xi + k_{n\eta}\mathbf{e}_\eta + k_{n\zeta}\mathbf{e}_\zeta$$

$$= k\left(v_\xi\right)_n \mathbf{e}_\xi + k\left(v_\eta\right)_n \mathbf{e}_\eta + k\mathbf{e}_\zeta, \tag{D3}$$

where $\mathbf{e}_j$ ($j = \xi,\ \eta,\ \zeta$) is the unit vector in the j-direction, $k = 2\pi n_0/\lambda$, and k_{nj} are components of the wave vector. Then, the angle of the oblique incidence is determined by the condition

$$\tan(\vartheta_n) = \frac{k_{n\perp}}{k} = \sqrt{\left(v_\xi\right)_n^2 + \left(v_\eta\right)_n^2}, \quad k_{n\perp} = \sqrt{k_{n\xi}^2 + k_{n\eta}^2}, \tag{D4}$$

$$\text{hence } \vartheta_n = \arctan\left(\sqrt{\left(v_\xi\right)_n^2 + \left(v_\eta\right)_n^2}\right).$$

Appendix E: Contact-type SMs

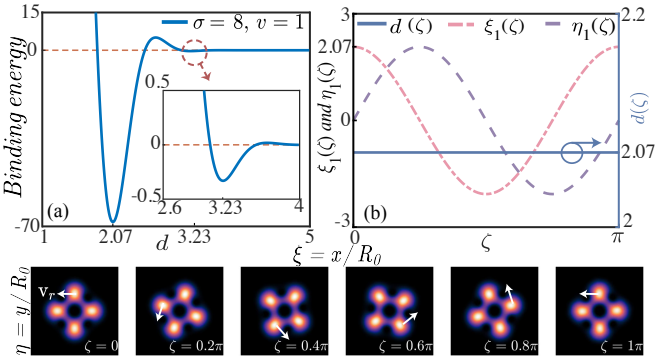


FIG. 9. (a) The BE exhibits two local minima at $d = 2.07$ and $d = 3.23$ in the strongly nonlocal regime. Inset: The second minimum in the BE aligns with the purple dashed-dotted line shown in Fig. 2(c). (b) The trajectory of the single soliton located at $(\xi_1, \eta_1) = (d, 0)$ with $d = 2.07$ is presented, along with the evolution of the center-of-mass position (ξ_1, η_1) and d, as functions of the propagation distance. (c) With the initial rotation velocity $v = 1$, the SM exhibits a counterclockwise rotational motion. The white arrows indicate how the tangent velocity of a particular soliton evolves during the propagation. As seen in the figure, adjacent solitons are connected by mutual interactions, the rotation period of the soliton being π. The other parameters are the same as Fig. 2(c).

According to the energy functional and BE equations, we find that more than one equilibrium point exists in the strongly nonlocal nonlinear regime. Here we focus on the first equilibrium position. When the soliton is placed at this position, with $d = 2.07$, and set in rotation by the initial tangent velocity $v = 1$, the resulting structure is a contact-type SM, as shown in Fig. 9(c). The other parameters $A = 4$, $a = 1$, and $b = 0$.

Next, we consider the SM's trajectory. Combining Eqs. (D2a) and (D2b), the trajectory of the center-of-mass of each constituent soliton in the (ξ, η) plane can be obtained:

$$\left[\left(v_\eta\right)_n(0)\xi_n - \left(v_\xi\right)_n(0)\eta_n\right]^2 + \beta_0^2\left[\eta_n(0)\xi_n - \xi_n(0)\eta_n\right]^2 = \left[\xi_n(0)\left(v_\eta\right)_n(0) - \eta_n(0)\left(v_\xi\right)_n(0)\right]^2. \tag{E1}$$

Taking the first soliton, initially located at $(\xi_1, \eta_1) = (d, 0)$, and substituting the input conditions in Eq. (E1), we obtain the standard ellipse:

$$v^2\xi_1^2(\zeta) + \eta_1^2(\zeta) = d^2v^2. \tag{E2}$$

Actually, all constituent solitons move along the same trajectory.

When $v = 1$, Eq. (E1) becomes the circle equation, $\xi_1^2 + \eta_1^2 = d^2$, with the circle's radius exactly equal to that of the initial ring. As shown by the blue solid line in Fig. 9(b), the circle's radius remains constant. The red doted-dashed and purple dashed lines trace the ξ_1 and η_1 trajectories, executing one full cosine and sine cycle, respectively, to confirm that the soliton follows a closed circular orbit.

In Fig. 9(c), one sees that adjacent solitons in the SM are connected through the mutual interactions, i.e., these are contact-type SM. As the tangent velocity is directed counterclockwise, the soliton SM rotates in that direction. The white arrows indicate how the soliton's tangent velocity evolves in the course of the propagation. As observed in the figure, the rotation period of each soliton is π.

[1] E. A. Kuznetsov, A. M. Rubenchik, and V. E. Zakharov, Soliton stability in plasmas and hydrodynamics, Phys. Rep. **142**, 103 (1986).

[2] W. Torruellas, Y. S. Kivshar, and G. I. Stegeman, *Spatial Solitons* (Springer Verlag, Berlin, 2001).

[3] A. Hasegawa, *Optical solitons in fibers* (Springer, Berlin, 2002).

[4] N. Akhmediev and A. Ankiewicz, *Dissipative Solitons* (Springer, Berlin, 2005).

[5] B. A. Malomed, *Soliton Management in Periodic Systems* (Springer, New York, 2006).

[6] F. Lederer, G. I. Stegeman, D. N. Christodoulides, G. Assanto, M. Segev, and Y. Silberberg, Discrete solitons in optics, Phys. Rep. **463**, 1 (2008).

[7] Y.-H. Jia, Z.-Z. Si, Z.-T. Ju, H.-Y. Feng, J.-H. Zhang, X. Yan, and C.-Q. Dai, Convolutional-recurrent neural network for the prediction of formation and switching dynamics for multicolor solitons, Sci. China-Phys. Mech. Astron. **68**, 284211 (2025).

[8] A. V. Ustinov, T. Doderer, R. P. Huebener, N. F. Pedersen, B. Mayer, and V. A. Oboznov, Dynamics of sine-Gordon solitons in the annular Josephson junction, Phys. Rev. Lett. **69**, 1815 (1992).

[9] A. Blanco-Redondo, C. M. de Sterke, C. Xu, S. Wabnitz, and S. K. Turitsyn, The bright prospects of optical solitons after 50 years, Nat. Photon. **17**, 937 (2023).

[10] Y. S. Kivshar and B. A. Malomed, Dynamics of solitons in nearly integrable systems, Rev. Mod. Phys. **61**, 763

(1989).
[11] K. Sakkaravarthi, R. Babu Mareeswaran, and T. Kanna, Bright matter-wave bound soliton molecules in spin-1 Bose-Einstein condensates with non-autonomous nonlinearities, Physica D **448**, 133694 (2023).
[12] A. S. Desyatnikov and Y. S. Kivshar, Rotating optical soliton clusters, Phys. Rev. Lett. **88**, 053901 (2002).
[13] B. A. Malomed, Bound solitons in the nonlinear Schrödinger-Ginzburg-Landau equation, Phys. Rev. A **44**, 6954 (1991).
[14] B. A. Malomed, Bound states of envelope solitons, Phys. Rev. A **47**, 2874 (1993).
[15] H. Sakaguchi, D. V. Skryabin, and B. A. Malomed, Stationary and oscillatory bound states of dissipative solitons created by the third-order dispersion, Opt. Lett. **43**, 2688 (2018).
[16] D. Y. Tang, W. S. Man, H. Y. Tam, and P. D. Drummond, Observation of bound states of solitons in a passively mode-locked fiber laser, Phys. Rev. A **64**, 033814 (2001).
[17] A. Komarov, K. Komarov, and F. Sanchez, Quantization of binding energy of structural solitons in passive mode-locked fiber lasers, Phys. Rev. A **79**, 033807 (2009).
[18] A. Gelash, D. Agafontsev, V. Zakharov, G. El, S. Randoux, and P. Suret, Bound state soliton gas dynamics underlying the spontaneous modulational instability, Phys. Rev. Lett. **123**, 234102 (2019).
[19] Y. Liu, S. Huang, Z. Li, H. Liu, Y. Sun, R. Xia, L. Yan, Y. Luo, H. Liu, G. Xu, Q. Sun, X. Tang, and P. P. Shum, Phase-tailored assembly and encoding of dissipative soliton molecules, Light Sci. Appl. **12**, 123 (2023).
[20] Y. Guo, W. Lin, W. Wang, R. Zhang, T. Liu, Y. Xu, X. Wei, and Z. Yang, Unveiling the complexity of spatiotemporal soliton molecules in real time, Nat. Commun. **14**, 2029 (2023).
[21] U. Al Khawaja, Interaction forces among two-dimensional bright solitons and many-soliton molecules, Phys. Rev. E **85**, 056604 (2012).
[22] L. Qin, C. Hang, B. A. Malomed, and G. Huang, Stable high-dimensional weak-light soliton molecules and their active control, Laser Photon. Rev. **16**, 2100297 (2022).
[23] J. Peng and H. Zeng, Build-Up of Dissipative Optical Soliton Molecules via Diverse Soliton Interactions, Laser Photon. Rev. **12**, 1800009 (2018).
[24] A. Zavyalov, R. Iliew, O. Egorov, and F. Lederer, Dissipative soliton molecules with independently evolving or flipping phases in mode-locked fiber lasers, Phys. Rev. A **80**, 043829 (2009).
[25] A. Boudjemaa and U. A. Khawaja, Stability of n-soliton molecules in dispersion-managed optical fibers, Phys. Rev. A **88**, 045801 (2013).
[26] W. Weng, R. Bouchand, E. Lucas, E. Obrzud, T. Herr, and T. J. Kippenberg, Heteronuclear soliton molecules in optical microresonators, Nat. Commun. **11**, 2402 (2020).
[27] A. Maitre, G. Lerario, A. Medeiros, F. Claude, Q. Glorieux, E. Giacobino, S. Pigeon, and A. Bramati, Dark-soliton molecules in an exciton-polariton superfluid, Phys. Rev. X **10**, 041028 (2020).
[28] K. Lakomy, R. Nath, and L. Santos, Soliton molecules in dipolar Bose-Einstein condensates, Phys. Rev. A **86**, 013610 (2012).
[29] W. E. Shirley, B. M. Anderson, C. W. Clark, and R. M. Wilson, Half-quantum vortex molecules in a binary dipolar Bose gas, Phys. Rev. Lett. **113**, 165301 (2014).
[30] V. Tsatourian, S. V. Sergeyev, C. Mou, A. Rozhin, V. Mikhailov, B. Rabin, P. S. Westbrook, and S. K. Turitsyn, Polarisation dynamics of vector soliton molecules in mode locked fibre laser, Sci. Rep. **3**, 3154 (2013).
[31] C. Yin, N. G. Berloff, V. M. Perez-Garcia, D. Novoa, A. V. Carpentier, and H. Michinel, Coherent atomic soliton molecules for matter-wave switching, Phys. Rev. A **83**, 051605 (2011).
[32] F. Kurtz, C. Ropers, and G. Herink, Resonant excitation and all-optical switching of femtosecond soliton molecules, Nat. Photon. **14**, 9 (2020).
[33] S. Liu, Y. Cui, E. Karimi, and B. A. Malomed, On-demand harnessing of photonic soliton molecules, Optica **9**, 240 (2022).
[34] F. Mitschke, A. Hause, and C. Mahnke, Soliton molecules for advanced optical telecommunications, Eur. Phys. J. Spec. Top. **225**, 2453 (2016).
[35] P. Rohrmann, A. Hause, and F. Mitschke, Two-soliton and three-soliton molecules in optical fibers, Phys. Rev. A **87**, 043834 (2013).
[36] S. M. Alamoudi, U. A. Khawaja, and B. B. Baizakov, Averaged dynamics of soliton molecules in dispersion-managed optical fibers, Phys. Rev. A **89**, 053817 (2014).
[37] P. Rohrmann, A. Hause, and F. Mitschke, Solitons beyond binary: Possibility of fibre-optic transmission of two bits per clock period, Sci. Rep. **2**, 866 (2012).
[38] P. Marin-Palomo, J. N. Kemal, M. Karpov, A. Kordts, J. Pfeifle, M. H. P. Pfeiffer, P. Trocha, S. Wolf, V. Brasch, M. H. Anderson, R. Rosenberger, K. Vijayan, W. Freude, T. J.Kippenberg, and C. Koos, Microresonator-based solitons for massively parallel coherent optical communications, Nature **546**, 274 (2017).
[39] Z.-Z. Si, Z.-T. Ju, L.-F. Ren, X.-P. Wang, B. A. Malomed, and C.-Q. Dai, Polarization-induced buildup and switching mechanisms for soliton molecules composed of noise-like-pulse transition states, Laser Photon. Rev. **19**, 2401019 (2025).
[40] H. Liu, Y. Luo, Y. Sun, Y. An, Y. Yao, J. Wang, C. Fan, Q. Sun, and P. P. Shum, Gain-dominated phase customization enables the hybrid quaternary encoding of dissipative soliton molecules, ACS Photon. **12**, 1601 (2025).
[41] Y. Yang, W. Lin, Y. Guo, X. Hu, H. Xu, D. Chen, X. Wei, and Z. Yang, Phase-encoding of loosely bound soliton molecules, APL Photon. **9**, 031305 (2024).
[42] X. Liu, Dynamic evolution of temporal dissipative-soliton molecules in large normal path-averaged dispersion fiber lasers, Phys. Rev. A **82**, 063834 (2010).
[43] C. Wang, L. Wang, X. Li, W. Luo, T. Feng, Y. Zhang, P. Guo, and Y. Ge, Few-layer bismuthene for femtosecond soliton molecules generation in Er-doped fiber laser, Nanotechnology **30**, 025204 (2019).
[44] L. Li, H. Huang, L. Su, D. Shen, D. Tang, M. Klimczak, and L. Zhao, Various soliton molecules in fiber systems, Appl. Opt. **58**, 2745 (2019).
[45] H. Qin, X. Xiao, P. Wang, and C. Yang, Observation of soliton molecules in a spatiotemporal mode-locked multimode fiber laser, Opt. Lett. **43**, 1982 (2018).
[46] Z. Q. Wang, K. Nithyanandan, A. Coillet, P. Tchofo-Dinda, and P. Grelu, Optical soliton molecular complexes in a passively mode-locked fibre laser, Nat. Commun. **10**, 830 (2019).
[47] J. Igbonacho, K. Nithyanandan, K. Krupa, P. Tchofo Dinda, P. Grelu, and A. B. Moubissi,

Dynamics of distorted and undistorted soliton molecules in a mode-locked fiber laser, Phys. Rev. A **99**, 063824 (2019).
[48] G. Xu, A. Gelash, A. Chabchoub, V. Zakharov, and B. Kibler, Breather wave molecules, Phys. Rev. Lett. **122**, 084101 (2019).
[49] M. Chen, S. Zeng, D. Lu, W. Hu, and Q. Guo, Optical solitons, self-focusing, and wave collapse in a space-fractional Schrödinger equation with a Kerr-type nonlinearity, Phys. Rev. E **98**, 022211 (2018).
[50] G. A. Askar'yan, *Effects of the gradient of a strong electromagnetic beam on electrons and atoms* (Springer, New York, 2008) p. 268.
[51] R. Y. Chiao, E. Garmire, and C. H. Townes, Self-trapping of optical beams, Phys. Rev. Lett. **13**, 479 (1964).
[52] P. Lallemand and N. Bloembergen, Self-focusing of laser beams and stimulated Raman gain in liquids, Phys. Rev. Lett. **15**, 1010 (1965).
[53] E. Garmire, R. Y. Chiao, and C. H. Townes, Dynamics and characteristics of the self-trapping of intense light beams, Phys. Rev. Lett. **16**, 347 (1966).
[54] A. W. Snyder and D. J. Mitchell, Accessible Solitons, Science **276**, 1538 (1997).
[55] W. Krolikowski and O. Bang, Solitons in nonlocal nonlinear media: Exact solutions, Phys. Rev. E **63**, 016610 (2000).
[56] C. Conti, M. Peccianti, and G. Assanto, Observation of optical spatial solitons in a highly nonlocal medium, Phys. Rev. Lett. **92**, 113902 (2004).
[57] Y. V. Kartashov, L.-C. Crasovan, D. Mihalache, and L. Torner, Robust propagation of two-color soliton clusters supported by competing nonlinearities, Phys. Rev. Lett. **89**, 273902 (2002).
[58] D. Mihalache, D. Mazilu, L.-C. Crasovan, B. A. Malomed, F. Lederer, and L. Torner, Robust soliton clusters in media with competing cubic and quintic nonlinearities, Phys. Rev. E **68**, 046612 (2003).
[59] L. Zeng, M. R. Belic, D. Mihalache, Q. Zhang, D. Xiang, and X. Zhu, Robust dynamics of soliton pairs and clusters in the nonlinear Schrödinger equation with linear potentials, Nonlinear Dyn. **111**, 21895 (2023).
[60] E. L. Falcao-Filho, C. B. de Araujo, G. Boudebs, H. Leblond, and V. Skarka, Robust two-dimensional spatial solitons in liquid carbon disulfide, Phys. Rev. Lett. **110**, 013901 (2013).
[61] P. Cheiney, C. R. Cabrera, J. Sanz, B. Naylor, L. Tanzi, and L. Tarruell, Bright soliton to quantum droplet transition in a mixture of Bose-Einstein condensates, Phys. Rev. Lett. **120**, 135301 (2018).
[62] B. A. Malomed, *Multidimensional Solitons* (AIP Publishing, 2022).
[63] O. Firstenberg, C. S. Adams, and S. Hofferberth, Nonlinear quantum optics mediated by Rydberg interactions, J. Phys. B **49**, 152003 (2016).
[64] T. F. Gallagher, *Rydberg Atoms* (Cambridge University Press, 2008).
[65] M. Saffman, T. G. Walker, and K. Molmer, Quantum information with Rydberg atoms, Rev. Mod. Phys. **82**, 2313 (2010).
[66] Z. Bai, C. S. Adams, G. Huang, and W. Li, Self-induced transparency in warm and strongly interacting Rydberg gases, Phys. Rev. Lett. **125**, 263605 (2020).
[67] C. Rotschild, B. Alfassi, O. Cohen, and M. Segev, Long-range interactions between optical solitons, Nat. Phys. **2**, 769 (2006).
[68] L. Qin, C. Hang, W. Li, and X. Zhao, Nonlinear Spin–Orbit Interaction of Light in a Cold Rydberg Atom Medium, Chin. Phys. Lett. **43**, 050303 (2026).
[69] L. Qin, S. Chen, L. Liu, H. Tian, Y. Zhang, Z. Shi, Z. Zhu, X. Zhao, and W. Liu, Higher-order exceptional points and asymmetric soliton scattering with triple-well PT-symmetry potential in an atomic gas, Front. Phys. **22**, 032202 (2027).
[70] C. Murray and T. Pohl, Quantum and nonlinear optics in strongly interacting atomic ensembles, in *Advances in Atomic, Molecular, and Optical Physics*, Vol. 65 (Academic Press, New York, 2016) pp. 321–372.
[71] J. D. Pritchard, K. J. Weatherill, and C. S. Adams, Nonlinear optics using cold Rydberg atoms, Annu. Rev. Cold At. Mol. **1**, 301 (2013).
[72] M. Fleischhauer, A. Imamoglu, and J. P. Marangos, Electromagnetically induced transparency: Optics in coherent media, Rev. Mod. Phys. **77**, 633 (2005).
[73] O. Firstenberg, T. Peyronel, Q. Y. Liang, A. V. Gorshkov, M. D. Lukin, and V. Vuletic, Attractive photons in a quantum nonlinear medium, Nature **502**, 71 (2013).
[74] Q.-Y. Liang, A. V. Venkatramani, S. H. Cantu, T. L. Nicholson, M. J. Gullans, A. V. Gorshkov, J. D. Thompson, C. Chin, M. D. Lukin, and V. Vuletić, Observation of three-photon bound states in a quantum nonlinear medium, Science **359**, 783 (2018).
[75] S. Baur, D. Tiarks, G. Rempe, and S. Dürr, Single-photon switch based on Rydberg blockade, Phys. Rev. Lett. **112**, 073901 (2014).
[76] A. V. Gorshkov, J. Otterbach, M. Fleischhauer, T. Pohl, and M. D. Lukin, Photon-photon interactions via Rydberg blockade, Phys. Rev. Lett. **107**, 133602 (2011).
[77] E. Shahmoon, G. Kurizki, M. Fleischhauer, and D. Petrosyan, Strongly interacting photons in hollow-core waveguides, Phys. Rev. A **83**, 033806 (2011).
[78] D. Chang, V. Gritsev, G. Morigi, V. Vuletić, M. Lukin, and E. Demler, Crystallization of strongly interacting photons in a nonlinear optical fibre, Nat. Phys. **4**, 884 (2008).
[79] M. O. Scully and M. S. Zubairy, *Quantum optics* (Cambridge University Press, 1997).
[80] Z. Bai, W. Li, and G. Huang, Stable single light bullets and vortices and their active control in cold Rydberg gases, Optica **6**, 309 (2019).
[81] F. Robicheaux, Calculations of long range interactions for 87Sr Rydberg states, J. Phys. B **52**, 244001 (2019).
[82] K. Guo, G. Wang, and A. Ye, Dipole polarizabilities and magic wavelengths for a Sr and Yb atomic optical lattice clock, J. Phys. B **43**, 135004 (2010).
[83] I. Tikhonenkov, B. A. Malomed, and A. Vardi, Anisotropic solitons in dipolar Bose-Einstein condensates, Phys. Rev. Lett. **100**, 090406 (2008).
[84] C. Hang, W. Li, and G. Huang, Nonlinear light diffraction by electromagnetically induced gratings with $\mathcal{PT}$ symmetry in a Rydberg atomic gas, Phys. Rev. A **100**, 043807 (2019).
[85] W. Krolikowski, O. Bang, J. J. Rasmussen, and J. Wyller, Modulational instability in nonlocal nonlinear kerr media, Phys. Rev. E **64**, 016612 (2001).
[86] M. Desaix, D. Anderson, and M. Lisak, Variational approach to collapse of optical pulses, J. Opt. Soc. Am. B **8**, 2082 (1991).
[87] L. Qin, C. Hang, Z. Shi, J. Qian, X. Feng, Y. Zhang,

S. Xia, Z. Zhu, W. Liu, and X. Zhao, Soliton molecules and their scattering by a localized PT-symmetric potential in atomic gases, Opt. Express **31**, 11116 (2023).

[88] J. Yang, *Nonlinear waves in integrable and nonintegrable systems* (SIAM, Philadelphia, 2010).

[89] G. Huang, L. Deng, and M. G. Payne, Dynamics of ultraslow optical solitons in a cold three-state atomic system, Phys. Rev. E **72**, 016617 (2005).

[90] C. Zhang, W. Lyu, L. Cong, Z. Gu, Z. Zhang, G. Wang, Y. Lyu, B. Yang, I. Ahmad, and B. Fu, Tunable soliton molecules enabled by a nanotubes-based mode-locked fiber laser, Front. Phys. **20**, 052201 (2025).

[91] D. Bohm, *Quantum Theory* (Courier Corporation, 2012).

[92] Y. Cui, Y. Zhang, L. Huang, A. Zhang, Z. Liu, C. Kuang, C. Tao, D. Chen, X. Liu, and B. A. Malomed, Dichromatic "breather molecules" in a mode-locked fiber laser, Phys. Rev. Lett. **130**, 153801 (2023).

[93] J. Peng, Z. Zhao, S. Boscolo, C. Finot, S. Sugavanam, D. V. Churkin, and H. Zeng, Breather molecular complexes in a passively mode-locked fiber laser, Laser Photon. Rev. **15**, 2000132 (2021).

[94] Q. Guo, B. Luo, F. Yi, S. Chi, and Y. Xie, Large phase shift of nonlocal optical spatial solitons, Phys. Rev. E **69**, 016602 (2004).

[95] B. Ortac, A. Zaviyalov, C. K. Nielsen, O. Egorov, R. Iliew, J. Limpert, F. Lederer, and A. Tunnermann, Observation of soliton molecules with independently evolving phase in a mode-locked fiber laser, Opt. Lett. **35**, 1578 (2010).

[96] A. S. Desyatnikov, D. Neshev, E. A. Ostrovskaya, Y. S. Kivshar, G. McCarthy, W. Krolikowski, and B. Luther-Davies, Multipole composite spatial solitons: theory and experiment, J. Opt. Soc. Am. B **19**, 586 (2002).

[97] H. Sakaguchi and B. A. Malomed, Higher-order vortex solitons, multipoles, and supervortices on a square optical lattice, Europhys. Lett. **72**, 698 (2005).

[98] L. Song, Z. Yang, X. Li, and S. Zhang, Controllable Gaussian-shaped soliton clusters in strongly nonlocal media, Opt. Express **26**, 19182 (2018).